



THE UNIVERSITY *of* EDINBURGH

Edinburgh Research Explorer

## Flagellated bacterial motility in polymer solutions

**Citation for published version:**

Martinez, VA, Schwarz-Linek, J, Reufer, M, Wilson, LG, Morozov, AN & Poon, WCK 2014, 'Flagellated bacterial motility in polymer solutions', *Proceedings of the National Academy of Sciences*, vol. 111, no. 50, pp. 17771-17776. <https://doi.org/10.1073/pnas.1415460111>

**Digital Object Identifier (DOI):**

[10.1073/pnas.1415460111](https://doi.org/10.1073/pnas.1415460111)

**Link:**

[Link to publication record in Edinburgh Research Explorer](#)

**Document Version:**

Publisher's PDF, also known as Version of record

**Published In:**

Proceedings of the National Academy of Sciences

**General rights**

Copyright for the publications made accessible via the Edinburgh Research Explorer is retained by the author(s) and / or other copyright owners and it is a condition of accessing these publications that users recognise and abide by the legal requirements associated with these rights.

**Take down policy**

The University of Edinburgh has made every reasonable effort to ensure that Edinburgh Research Explorer content complies with UK legislation. If you believe that the public display of this file breaches copyright please contact [openaccess@ed.ac.uk](mailto:openaccess@ed.ac.uk) providing details, and we will remove access to the work immediately and investigate your claim.



# Flagellated bacterial motility in polymer solutions

Vincent A. Martinez<sup>a,1</sup>, Jana Schwarz-Linek<sup>a</sup>, Mathias Reufer<sup>a</sup>, Laurence G. Wilson<sup>b,c</sup>, Alexander N. Morozov<sup>a</sup>, and Wilson C. K. Poon<sup>a</sup>

<sup>a</sup>Scottish Universities Physics Alliance (SUPA), School of Physics and Astronomy, University of Edinburgh, Edinburgh EH9 3FD, United Kingdom; <sup>b</sup>Department of Physics, University of York, York YO10 5DD, United Kingdom; and <sup>c</sup>The Rowland Institute at Harvard, Cambridge, MA 02142

Edited by Tom C. Lubensky, University of Pennsylvania, Philadelphia, PA, and approved October 28, 2014 (received for review August 15, 2014)

It is widely believed that the swimming speed,  $v$ , of many flagellated bacteria is a nonmonotonic function of the concentration,  $c$ , of high-molecular-weight linear polymers in aqueous solution, showing peaked  $v(c)$  curves. Pores in the polymer solution were suggested as the explanation. Quantifying this picture led to a theory that predicted peaked  $v(c)$  curves. Using high-throughput methods for characterizing motility, we measured  $v$  and the angular frequency of cell body rotation,  $\Omega$ , of motile *Escherichia coli* as a function of polymer concentration in polyvinylpyrrolidone (PVP) and Ficoll solutions of different molecular weights. We find that nonmonotonic  $v(c)$  curves are typically due to low-molecular-weight impurities. After purification by dialysis, the measured  $v(c)$  and  $\Omega(c)$  relations for all but the highest-molecular-weight PVP can be described in detail by Newtonian hydrodynamics. There is clear evidence for non-Newtonian effects in the highest-molecular-weight PVP solution. Calculations suggest that this is due to the fast-rotating flagella seeing a lower viscosity than the cell body, so that flagella can be seen as nano-rheometers for probing the non-Newtonian behavior of high polymer solutions on a molecular scale.

swimming microorganisms | complex fluids | rheology | non-Newtonian fluids

The motility of microorganisms in polymer solutions is a topic of vital biomedical interest. For example, mucus covers the respiratory (1), gastrointestinal (2), and reproductive (3) tracks of all metazoans. Penetration of this solution of biomacromolecules by motile bacterial pathogens is implicated in a range of diseases, e.g., stomach ulcers caused by *Helicobacter pylori* (4). Oviduct mucus in hens provides a barrier against *Salmonella* infection of eggs (5). Penetration of the exopolysaccharide matrix of biofilms by swimming bacteria (6) can stabilize or destabilize them in vivo (e.g., the bladder) and in vitro (e.g., catheters). In reproductive medicine (human and veterinary), the motion of sperms in seminal plasma and vaginal mucus, both non-Newtonian polymer solutions, is a strong determinant of fertility (3), and polymeric media are often used to deliver spermicidal and other vaginal drugs (7).

Microorganismic propulsion in non-Newtonian media such as high-polymer solutions is also a hot topic in biophysics, soft matter physics, and fluid dynamics (8). Building on knowledge of propulsion modes at low Reynolds number in Newtonian fluids (8), current work seeks to understand how these are modified to enable efficient non-Newtonian swimming. In particular, there is significant interest in a flapping sheet (9, 10) or an undulating filament (11) (modeling the sperm tail) and in a rotating rigid helix (modeling the flagella of, e.g., *Escherichia coli*) (12, 13) in non-Newtonian fluids.

An influential set of experiments in this field was performed 40 years ago by Schneider and Doetsch (SD) (14), who measured the average speed,  $\bar{v}$ , of seven flagellated bacterial species (including *E. coli*) in solutions of polyvinylpyrrolidone (PVP, molecular weight given as  $M=360$  kDa) and in methyl cellulose (MC,  $M$  unspecified) at various concentrations,  $c$ . SD claimed that  $\bar{v}(c)$  was always nonmonotonic and peaked.

A qualitative explanation was suggested by Berg and Turner (BT) (15), who argued that entangled linear polymers formed “a loose quasi-rigid network easily penetrated by particles of microscopic size.” BT measured the angular speed,  $\Omega$ , of the

rotating bodies of tethered *E. coli* cells in MC solutions. They found that adding MC hardly decreased  $\Omega$ . However, in solutions of Ficoll, a branched polymer,  $\Omega$  is proportional to  $\eta^{-1}$ , where  $\eta$  is the solution’s viscosity, which was taken as evidence for Newtonian behavior. In MC solutions, however, BT suggested that there were *E. coli*-sized pores, so that cells rotated locally in nearly pure solvent. Magariyama and Kudo (MK) (16) formulated a theory based on this picture and predicted a peak in  $v(c)$  by assuming that a slender body in a linear-polymer solution experienced different viscosities for tangential and normal motions in BT’s “easily penetrated” pores.

This standard model is widely accepted in the biomedical literature on flagellated bacteria in polymeric media. It also motivates much current physics research in non-Newtonian low-Reynolds-number propulsion. Nevertheless, there are several reasons for a fundamental reexamination of the topic.

First, polymer physics (17) casts a priori doubt on the presence of *E. coli*-sized pores in an entangled solution. Entanglement occurs above the overlap concentration,  $c^*$ , where coils begin to touch. The mesh size at  $c^*$ , comparable to a coil’s radius of gyration,  $r_g$ , gives the maximum possible pore size in the entangled network. For 360-kDa PVP in water,  $r_g \lesssim 60$  nm (see below), which is well under the cross section of *E. coli* (0.8  $\mu\text{m}$ ). Thus, the physical picture suggested by BT (15) and used by MK (16) has doubtful validity.

Second, SD’s data were statistically problematic. They took movies, from which cells with “the 10 greatest velocities were used to calculate the average velocity” (14). Thus, their peaks in  $v(c)$  could be no more than fluctuations in measurements that were in any case systematically biased.

Finally, although MK’s theory indeed predicts a peak in  $v(c)$ , we find that their formulas also predict a monotonic increase in

## Significance

The way microorganisms swim in concentrated polymer solutions has important biomedical implications, i.e., how pathogens invade the mucosal lining of mammal guts. Physicists are also fascinated by self-propulsion in such complex non-Newtonian fluids. The current standard model of how bacteria propelled by rotary helical flagella swim through concentrated polymer solutions postulates bacteria-sized pores, allowing them relative easy passage. Our experiments using high-throughput methods overturn this standard model. Instead, we show that the peculiarities of flagellated bacteria locomotion in concentrated polymer solutions are due to the fast-rotating flagellum, giving rise to a lower local viscosity in its vicinity. The bacterial flagellum is therefore a nano-rheometer for probing flows at the molecular level.

Author contributions: V.A.M. and W.C.K.P. designed research; V.A.M., J.S.-L., M.R., and A.N.M. performed research; V.A.M. and L.G.W. contributed new reagents/analytic tools; V.A.M., J.S.-L., M.R., A.N.M., and W.C.K.P. analyzed data; and V.A.M., A.N.M., and W.C.K.P. wrote the paper.

The authors declare no conflict of interest.

This article is a PNAS Direct Submission.

<sup>1</sup>To whom correspondence should be addressed. Email: vincent.martinez@ed.ac.uk.

This article contains supporting information online at [www.pnas.org/lookup/suppl/doi:10.1073/pnas.1415460111/-DCSupplemental](http://www.pnas.org/lookup/suppl/doi:10.1073/pnas.1415460111/-DCSupplemental).

$\Omega(c)$  in the same range of  $c$  (Fig. S1), which is inconsistent with the data of BT, who observed a monotonic decrease.

We therefore performed a fresh experimental study of *E. coli* motility using the same polymer (PVP) as SD, but varying the molecular weight,  $M$ , systematically. High-throughput methods for determining  $v$  and  $\Omega$  enabled us to average over  $\sim 10^4$  cells at each data point. Using polymers as purchased, we indeed found peaked  $v(c)$  curves at all  $M$  studied. However, purifying the polymers removed the peak in all but a single case. Newtonian hydrodynamics can account in detail for the majority of our results, collapsing data onto master curves. We show that the ratio  $v(c)/\Omega(c)$  is a sensitive indicator of non-Newtonian effects, which we uncover for 360-kDa PVP. We argue that these are due to shear-induced changes in the polymer around the flagella.

Below, we first give the necessary theoretical and experimental background before reporting our results.

### Theoretical Groundwork: Solving Purcell's Model

Purcell's widely used "model *E. coli*" has a prolate ellipsoidal cell body bearing a single left-handed helical flagellum at one pole (18). Its motion is described by three kinematic parameters: the swimming speed,  $v$ , the flagellum angular speed,  $\omega$ , and the body angular speed,  $\Omega$ ,

$$\mathbf{v} = (v, 0, 0), \quad \boldsymbol{\omega} = (-\omega, 0, 0), \quad \boldsymbol{\Omega} = (\Omega, 0, 0), \quad [1]$$

with  $(v, \omega, \Omega) > 0$ . The drag forces and torques ( $\mathbb{F}, \mathbb{N}$ ) on the body (subscript  $b$ ) and flagellum (subscript  $f$ ) are given by

$$\begin{pmatrix} \mathbb{F}_b \\ \mathbb{N}_b \end{pmatrix} = - \begin{pmatrix} A_0 & 0 \\ 0 & D_0 \end{pmatrix} \begin{pmatrix} \mathbf{v} \\ \boldsymbol{\Omega} \end{pmatrix}, \quad [2]$$

$$\begin{pmatrix} \mathbb{F}_f \\ \mathbb{N}_f \end{pmatrix} = - \begin{pmatrix} A & B \\ B & D \end{pmatrix} \begin{pmatrix} \mathbf{v} \\ \boldsymbol{\omega} \end{pmatrix}, \quad [3]$$

where  $A_0, D_0, A, B, D \propto \eta_s$ , the solvent viscosity. Requiring the body and flagellum to be force and torque free, we find

$$\Omega = \frac{D(A_0 + A) - B^2}{D_0(A + A_0)} \omega \equiv \beta \omega, \quad [4]$$

$$v = \frac{B}{A_0 + A} \omega \equiv \gamma \omega, \quad [5]$$

where  $\beta$  and  $\gamma$  are viscosity-independent geometric constants. Eqs. 4 and 5 predict that

$$\Omega = R_1 v, \quad \text{with} \quad R_1 = \beta/\gamma, \quad [6]$$

but underdetermine  $(v, \Omega, \omega)$ . Closure requires experimental input, in the form of the relationship between the torque developed by the motor,  $N$ , and its angular speed,  $\omega_m$ , where

$$\omega_m = \Omega + \omega = (1 + \beta^{-1})\Omega. \quad [7]$$

Measurements have repeatedly shown (19) that  $N(\omega_m)$  displays two regimes (Fig. 1), which we model as

$$\omega \leq \omega_m^c : N = N_0 \quad [8a]$$

$$\omega > \omega_m^c : N = \alpha(\omega_m^{\max} - \omega_m), \quad [8b]$$

where  $\alpha = |dN/d\omega_m| = N_0/(\omega_m^{\max} - \omega_m^c)$  is the absolute slope of  $N(\omega_m)$  when  $\omega_m^c < \omega < \omega_m^{\max}$ . For our purposes later, it is important to realize that Eq. 7 implies an equivalent  $N(\Omega)$  relation, with associated  $\Omega^c$  and  $\Omega^{\max}$ .

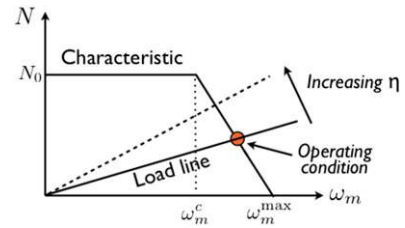


Fig. 1. Schematic of the relationship  $N(\omega_m)$  between the flagellum motor torque,  $N$ , and its angular speed,  $\omega_m$ . Intersection with a load-line determines the operating condition. The  $N(\Omega)$  relation has the same form (cf. Eq. 7).

Eqs. 4, 5, 8a, and 8b completely specify the problem. We can now predict  $\Omega$  and  $v = \Omega/R_1$ , the observables in this work, as functions of solvent viscosity by noting that the motor torque is balanced by the drag torque on the body

$$N = D_0 \Omega = \left( \frac{D_0}{1 + \beta^{-1}} \right) \omega_m. \quad [9]$$

Eq. 9 specifies a load line that intersects with the motor characteristic curve (Fig. 1) to determine the operating condition. For a prolate ellipsoidal cell body with semimajor and semiminor axes  $a$  and  $b$ ,  $D_0 = 16\pi\eta a b^2/3$ , so that

$$\omega < \omega_m^c : \Omega = \frac{N_0}{D_0} = \left( \frac{3N_0}{16\pi a b^2} \right) \eta^{-1} \quad [10a]$$

$$\omega > \omega_m^c : \Omega = \frac{\alpha^* \Omega^{\max}}{\alpha^* + D_0} = \frac{3\alpha^* \Omega^{\max} \eta^{-1}}{16\pi a b^2 + 3\alpha^* \eta^{-1}}, \quad [10b]$$

where  $\alpha^* = |dN/d\Omega| = N_0/(\Omega^{\max} - \Omega^c)$  is the absolute slope of the  $N(\Omega)$  relation (cf Fig. 1) in the variable-torque regime.

Recall that BT equated  $\Omega \propto \eta^{-1}$  scaling with Newtonian behavior (15). The above results show that this is true in the constant-torque regime ( $\omega < \omega_m^c$ ) of the motor. Our experiments demonstrate that this is not the only relevant regime.

### Experimental Groundwork: Characterizing Polymers

SD used "PVP K-90, molecular weight 360,000" (14), which, according to current standards (20), has a number averaged molecular weight of  $M_n = 360$  kDa, and a weight-average molecular weight of  $M_w \approx 10^6$  kDa. We show in SI Text that SD's polymer probably has somewhat lower  $M_w$  than the current PVP 360 kDa. We used four PVPs (Sigma Aldrich) with stated average molecular weights of  $M \sim 10$  kDa (no K-number given), 40 kDa (K-30), 160 kDa (K-60), and 360 kDa (K-90). Measured low-shear viscosities, which obeyed a molecular weight scaling consistent with good solvent conditions, yielded (see SI Text for details) the overlap concentrations (17),  $c^* = 0.55 \pm 0.01, 1.4 \pm 0.02, 3.8 \pm 0.1, \text{ and } 9.5 \pm 0.5$  wt.% (in order of decreasing  $M$ ; Fig. S2 and Table S1). Static light scattering in water gave  $M_w \approx 840$  kDa for our PVP360k, well within the expected range (20), and  $r_g = 56$  nm (Table S2). We also used Ficoll with  $M \sim 70$  kDa and 400 kDa from Sigma Aldrich (Fi70k, Fi400k).

### Results

We measured the motility of *E. coli* in polymer solutions using two new high-throughput methods (*Materials and Methods* and SI Text). Differential dynamic microscopy (DDM), which involves correlating Fourier-transformed images in time, delivers, *inter alia*, the mean swimming speed  $\bar{v}$  (21, 22). In dark-field flicker microscopy (DFM), we average the power spectrum of the flickering dark-field image of individual swimmers to obtain the mean body angular speed,  $\bar{\Omega}$ .

Cells suspended in a phosphate motility buffer were mixed with polymer solution in buffer to reach final desired concentrations and loaded into sealed capillaries for DDM and DFM. The concentrations of cells were low enough to avoid any cell-cell interaction, including polymer-induced depletion aggregation (23)—the absence of the latter being confirmed by microscopy. Separate experiments confirmed that oxygen depletion is negligible over the duration of the measurements.

**Native Polymer.** The measured  $\bar{v}(c)$  curves for all four PVP (Fig. S3) and Ficoll (Fig. S4) solutions are all nonmonotonic. The peak we see in PVP360k (Fig. S3) is somewhat reminiscent of SD's observation (14) for *E. coli* (Fig. 2A). Interestingly, all  $\bar{\Omega}(c)$  are also nonmonotonic except for PVP360k (Fig. S3).

**Dialyzed Polymers.** The initial rise in  $\bar{v}$  and  $\bar{\Omega}$  on addition of native polymers (Figs. S3 and S4) are somewhat reminiscent of the way swimming speed of *E. coli* rises on adding small-molecule carbon sources (see the example of glycerol in Fig. S5), which cells take up and metabolize to increase the proton motive force. PVP is highly efficient in complexing with various small molecules (20). We therefore cleaned the as-bought, native polymers by repeated dialysis using membranes that should remove low-molecular-weight impurities (Materials and Methods) and then repeated the  $\bar{v}(c)$  and  $\bar{\Omega}(c)$  measurements (Fig. 2), now reported in normalized form,  $\bar{v}/\bar{v}_0$  and  $\bar{\Omega}/\bar{\Omega}_0$ , with  $\bar{v}_0$  and  $\bar{\Omega}_0$  values at  $c = 0$  (buffer).

The prominent broad peaks or plateaus seen in the data for native PVP40k and PVP160k have disappeared (the same is true for Fi70k and Fi400k; Fig. S6). A small bump (barely one error bar high) in the data for PVP10k remains. Given the flatness of the data in PVP40k and PVP160k, we believe that the residual peak in PVP10k, whose coils have higher surface to volume ratio, is due to insufficient cleaning. A small peak ( $\lesssim 10\%$  increase) in  $\bar{v}(c)/\bar{v}_0$  also remains for PVP360k. For now, what most obviously distinguishes the PVP360k from the other three polymers is that the normalized  $\bar{v}(c)$  and  $\bar{\Omega}(c)$  for the latter coincide over the whole  $c$  range, whereas for PVP360k, they diverge from each other at all but the lowest  $c$ .

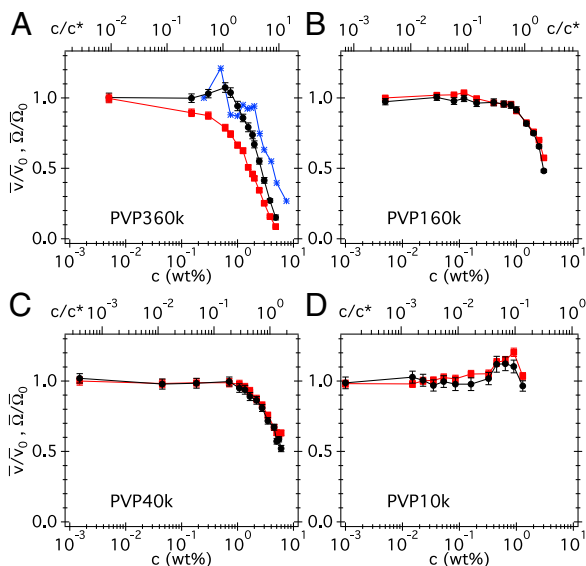


**Fig. 2.** (A–D) Normalized swimming speed  $\bar{v}/\bar{v}_0$  (black circles) and body angular speed  $\bar{\Omega}/\bar{\Omega}_0$  (red squares) vs. dialyzed PVP concentration (in weight percent) at four molecular weights, with  $\bar{v}_0 \approx 15 \mu\text{m/s}$  and  $\bar{\Omega}_0 \approx 20 \text{ Hz}$ . Top axis: PVP concentration normalized to  $c^*$ . The blue stars in A are the swimming speeds from SD (14) normalized to the values at their lowest polymer concentration.

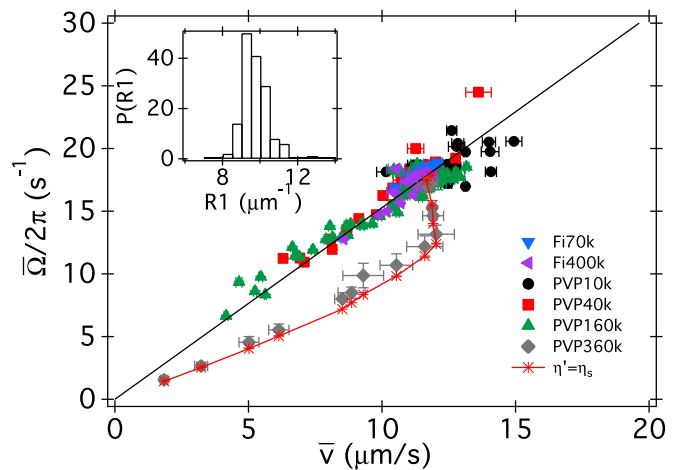


**Fig. 3.** Mean rotational frequency  $\bar{\Omega}/2\pi$  vs. swimming speed  $\bar{v}$  for dialyzed PVP and Ficoll solutions at molecular weights as indicated (there are at least two datasets per each PVP and one dataset for each Ficoll). The line is a linear fit to all data (except PVP360k), giving  $R_1 = 9.6 \pm 0.1 \mu\text{m}^{-1}$  in Eq. 6. (Inset) Probability distribution of  $R_1$  for all datasets except PVP360k. The diamonds are for PVP360k averaged over two datasets with the error bars being SDs. The stars linked by the full curve are the predicted  $\Omega(v)$  for PVP360k, according to a model in which the body experiences the full low-shear viscosity of the polymer solution, and the flagella experiences the viscosity of pure buffer,  $\eta_s$ .

**Newtonian Propulsion.** To observe  $\bar{v}(c)/\bar{v}_0 = \bar{\Omega}(c)/\bar{\Omega}_0$  (Fig. 2 B–D) we require  $\bar{v} \propto \bar{\Omega}$ , i.e., that Eq. 6 should be valid. This proportionality is directly confirmed by Fig. 3: data for PVP10k, 40k, and 160k collapse onto a single master proportionality at all concentrations. Data for two dialyzed Ficolls also fall on the same master line. The good data collapse shows that there is only very limited sample-to-sample variation in the average body and flagellar geometry, which are the sole determinants of  $R_1$  in Eq. 6. The slope of the line fitted to all of the data gives  $R_1 \approx 9.6 \mu\text{m}^{-1}$  (compare  $\approx 7 \mu\text{m}^{-1}$  in ref. 24). The constancy of the ratio  $R_1 = \bar{\Omega}/\bar{v}$  is also seen from the strongly peaked distribution of this quantity calculated from all individual pairs of  $\bar{v}(c)$  and  $\bar{\Omega}(c)$  values except those for PVP360k (Fig. 3, Inset). Physically,  $R_1$  is an inverse cell body processivity, i.e., on average a bacterium swims forward a distance  $R_1^{-1} \approx 0.1 \mu\text{m}$  per body revolution.

The implication of Fig. 3 is that swimming *E. coli* sees all our polymer solutions except PVP360k as Newtonian fluids. Interestingly, BT cited the proportionality between  $\bar{\Omega}$  and  $\eta^{-1}$  (rather than  $\bar{\Omega}$  and  $\bar{v}$ ) as evidence of Newtonian behavior in Ficoll. We show the dependence of body rotation speed normalized by its value at no added polymer,  $\bar{\Omega}/\bar{\Omega}_0$ , on the normalized fluidity  $\eta_s/\eta$  (where  $\eta_s$  is the viscosity of the solvent, i.e., buffer) for our four PVPs and two Ficolls in Fig. 4, together with the lines used by BT to summarize their MC and Ficoll data. Our data and BT's MC results (which span  $0.2 \lesssim \eta_s/\eta < 1$ ) cluster around a single master curve, which, however, is not a simple proportionality. Eqs. 10a and 10b together predict such nonlinear data collapse, provided that the cell body geometry,  $(a, b)$ , and the motor characteristics,  $(N_0, \Omega^c, \Omega^{\text{max}})$ , remain constant between datasets. The larger data scatter in Fig. 4 compared with Fig. 3 suggests somewhat larger variations in motor characteristics than in geometry between samples.\*

\*Note, however, that this refers to the fictitious effective motor powering the single effective flagellum in Purcell's *E. coli* model, so that in reality, the variability may reflect differing number and spatial distribution of flagella as much as individual motor characteristics.

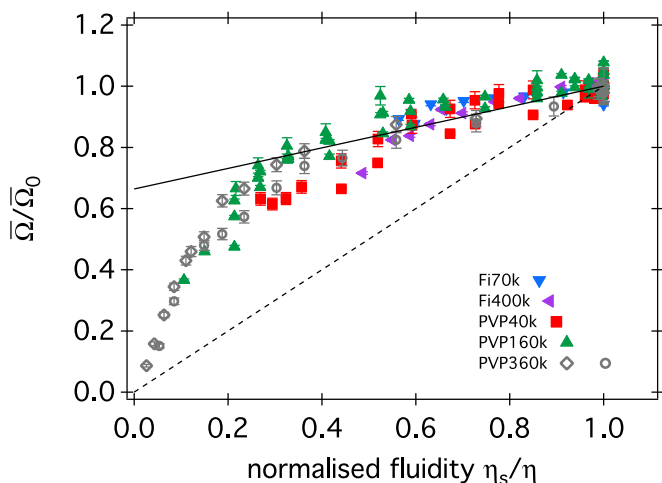


**Fig. 4.** Relative rotational body speed  $\bar{\Omega}/\bar{\Omega}_0$  vs. fluidity ( $1/\eta$ ), normalized to the fluidity of the motility buffer ( $c = 0$ ), for all polymer solutions we studied. Full and dashed lines are those used by BT to summarize their MC and Ficolli data, respectively. BT's MC data spanned a smaller interval ( $0.2 \lesssim \eta_s/\eta < 1$ ) than ours.

Of all of the polymers contributing to Fig. 4, PVP360k gave the most extensive coverage over the whole range of fluidity (Fig. 5).<sup>†</sup> Eqs. **10a** and **10b** apply to the low and high fluidity regimes of these data, respectively. Eq. **10a** depends on a single motor parameter,  $N_0$ , and predicts a strict proportionality. Our lowest fluidity data points suggest that at the highest polymer concentrations reached, we are indeed operating in this regime. Using  $a = 1.2 \mu\text{m}$  and  $b = 0.43 \mu\text{m}$  (average values from microscopy) to fit Eq. **10a** to the lowest fluidity data gives  $N_0 = 1,450 \pm 50 \text{ pN}\cdot\text{nm}$  (Fig. 5, blue), which agrees well with previously measured stall torque (19).

The majority of the data away from the lowest fluidities are clearly nonlinear and need to be fitted with Eq. **10b**. Doing so with the above value of  $N_0$  gives  $\bar{\Omega}^c/2\pi = 6.6 \pm 0.5 \text{ s}^{-1}$  and  $\bar{\Omega}^{\text{max}}/2\pi = 20.5 \pm 0.5 \text{ s}^{-1}$  (Fig. 5, pink). Given that  $\Omega \propto \omega_m$  (Eq. 7), we expect  $\bar{\Omega}^{\text{max}}/\bar{\Omega}^c = \omega_m^{\text{max}}/\omega_m^c$ . Our ratio of  $\bar{\Omega}^{\text{max}}/\bar{\Omega}^c \approx 3.1$  compares reasonably with  $\omega_m^{\text{max}}/\omega_m^c \approx 2.3$  for a different strain of *E. coli* at the same temperature (22 °C) (19).

Thus, Eqs. **10a** and **10b** give a reasonable account of the data in Fig. 5. We conclude that PVP360k solution is Newtonian as far as body rotation is concerned.

**Non-Newtonian Effects and Flagella Nano-Rheology.** Given the above conclusion, the nonlinear  $\bar{\Omega}(\bar{v})$  for PVP360k (Fig. 3) suggests a non-Newtonian response at the flagellum. In a minimal model, the flagellum “sees” a different viscosity,  $\eta'(c)$ , than the cell body, which simply experiences the low-shear viscosity of the polymer solution,  $\eta(c)$ . Making explicit the viscosity dependence of the resistive coefficients in Eqs. **2** and **3** by writing  $A = \hat{a}\eta$ , etc., force and torque balance now read

$$\eta \hat{a}_0 v = \eta' (-\hat{a} v + \hat{b} \omega), \quad [11]$$

$$\eta \hat{d}_0 \Omega = \eta' (-\hat{b} v + \hat{d} \omega). \quad [12]$$

Solving these gives

<sup>†</sup>To reach lower fluidity, or higher viscosity, required progressively more polymer (by mass). To recover enough polymer after dialysis becomes more challenging as the molecular weight decreases.

$$\frac{\bar{\Omega}}{v} = \frac{\hat{d} \left[ \left( \frac{\eta}{\eta'} \right) \hat{a}_0 + \hat{a} \right] - \hat{b}^2}{\left( \frac{\eta}{\eta'} \right) \hat{d}_0 \hat{b}}. \quad [13]$$

Eq. **11** makes an interesting prediction. If we take  $\eta'(c) = \eta_s$  and use previously quoted flagellum dimensions for *E. coli* (24) to calculate  $(\hat{a}_0, \hat{d}_0; \hat{a}, \hat{b}, \hat{d})$ , it predicts nearly perfectly the observed nonlinear  $\bar{\Omega}(\bar{v})$  relationship for PVP360k (Fig. 3). Details are given in *SI Text*, where we also predict the observed peak in  $\bar{v}(c)$  (Fig. 2 and Fig. S7). To check consistency, we proceed in reverse and treat the flagellum as a nano-rheometer. Given the measured  $\bar{v}(c)$  in PVP360k, we deduce the viscosity seen by the flagellum,  $\eta'(c)$ , at shear rate  $\dot{\gamma} \approx 10^4 \text{ s}^{-1}$  (*SI Text* and Fig. 6). In Fig. 6 we also show the low-shear viscosity of PVP360k solutions measured using conventional rheometry. Indeed, over most of the concentration range, we find  $\eta' \approx \eta_s$ . (Note that the highest  $c$  data points are subject to large uncertainties associated with measuring very low swimming speeds.) Thus, our data are consistent with the flagellum seeing essentially just the viscosity of the pure solvent (buffer). Macroscopically, this corresponds to extreme shear thinning. Is this a reasonable interpretation?

For a helical flagellum of thickness  $d$  and diameter  $D$  rotating at angular frequency  $\omega$ , the local shear rate is  $\dot{\gamma}_f \sim \omega D/d$  (we neglect translation because  $v \ll \omega D$ ). For an *E. coli* flagellar bundle,  $d \approx 40 \text{ nm}$ ,  $D \approx 550 \text{ nm}$ , and  $\omega \approx 2\pi \times 115 \text{ rad/s}$  (24), giving  $\dot{\gamma}_f \lesssim 10^4 \text{ s}^{-1}$  in the vicinity of the flagellum. The Zimm relaxation time of a polymer coil is  $\tau_Z \sim 4\pi\eta_s r_g^3/k_B T$ , where  $k_B T$  is the thermal energy. Using  $\eta_s = 10^{-3} \text{ Pa}\cdot\text{s}$  and  $r_g \approx 60 \text{ nm}$ , we find  $\tau_Z \sim 1 \text{ ms}$  for our PVP360k at room temperature. Because  $\Omega^{-1} \gg \tau_Z$ , the cell body does not perturb significantly the polymer conformation. However,  $\dot{\gamma}_f^{-1} \sim 0.1\tau_Z$ , so that the polymer may be expected to shear thin in both dilute ( $c < c^*$ ) (25) and semidilute ( $c \gtrsim c^*$ ) (26) solutions. Low-shear rate data collected using rheometry and high-frequency microrheological data collected using 1- $\mu\text{m}$  beads and interpreted using the Cox–Merz rule (27) (see *SI Text* for details) show that there is indeed significant shear thinning of our PVP360k polymer (Fig. 6 and Fig. S8), although not as extreme as thinning down to  $\eta_s$ .

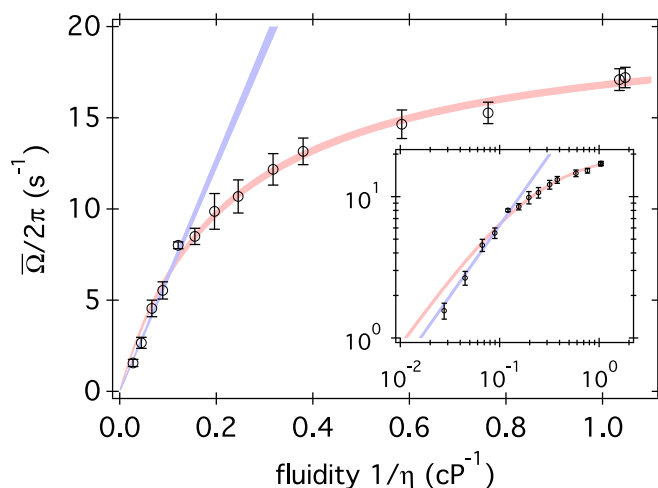


**Fig. 5.** Body rotation frequency vs. fluidity averaged over all PVP360k datasets. Blue line, fitting the constant-torque result, Eq. **10a**, in the range  $0 \leq \eta \leq 0.15 \text{ cP}^{-1}$ . Pink curve, fitting the linear-torque result, Eq. **10b**, in the range  $\eta \gtrsim 0.2 \text{ cP}^{-1}$ . The thickness of the line/curve indicates uncertainties associated with choosing the boundary between the two kinds of behavior. (Inset) Log-log plot to show that Eq. **10b** alone does not fit the data.

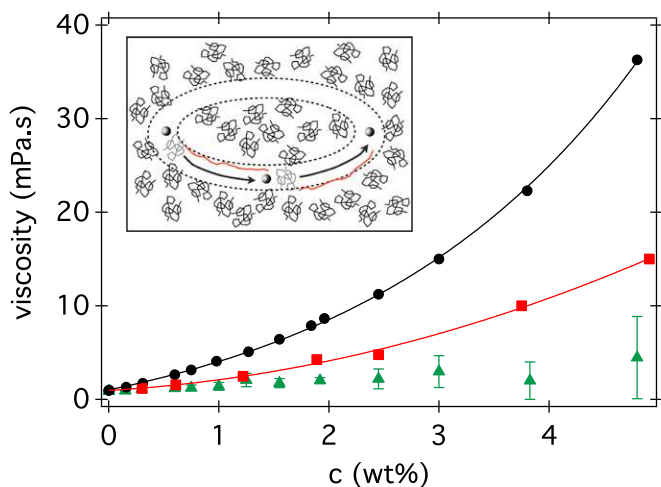


**Fig. 6.** Viscosities of PVP360k solutions: low-shear values from rheometry (filled circle); microrheology data obtained using 980-nm beads at  $10^4$  Hz (red square); and  $\eta'$  deduced from swimming data (green triangle). Lines are best fits (SI Text). (Inset) Schematic showing three snapshots of a section of a flagellum (sphere,  $\approx 40$  nm) cutting through a solution of polymer coils ( $\approx 120$  nm) (with a circular path). Coils, which are initially in the path of the flagellum section (gray), become stretched out (red), leaving a coil-sized channel of solvent.

Anisotropic elastic stresses (9–11, 13) and shear thinning (28, 29) have been proposed before as a possible cause of non-Newtonian effects in biological swimmers. However, in the usual sense, these are continuum concepts arising from experiments on the millimeter (rheometry) or micrometer (microrheology) scale. Neither is obviously applicable to an  $\sim 40$ -nm segment of flagellum moving through somewhat larger polymer coils ( $r_g \sim 60$  nm). One of the very few explorations of the  $\dots$  probe  $\sim$  polymer size regime to date found a highly nonlinear time dependent response with a shear-thinning steady state that matched bulk rheometry data, albeit with quite stiff polymers ( $\lambda$ -phage DNA) (30). The relevant physics may be similar to, but perhaps more complex than, the active microrheology of colloidal suspensions using probes that are approximately the same size as the colloids (31). A qualitative picture (Fig. 6, Inset) may be as follows. A section of the flagellum traveling at  $\omega D/2 \sim 200 \mu\text{m/s}$  takes  $\sim 0.3\tau_Z$  to traverse  $\sim r_g$ . Thus, polymer coils in its vicinity are strongly stretched as quasi-stationary objects and the flagellum effectively carves out an  $\sim 2r_g$ -wide channel practically void of polymers. Each flagellum section revisits approximately the same spatial location with a period  $2\pi/\omega \sim 10$  ms (because the translation per turn is low). Although this time is larger than the single chain relaxation time  $\tau_Z$ , the time required for collective relaxation and diffusion of a large number of strongly stretched polymer chains is significantly larger than that. Effectively, then, the flagellum moves inside a channel with viscosity  $\rightarrow \eta_s$ . Moreover, under strong local elongation of the kind we suggested, it is also possible that polymers may break (32). This separate, but related, mechanism could change the mechanical properties of the solution around the flagellum.

We note that previous experiments of *E. coli* swimming in MC (15, 33) used polymers and worked in concentration regimes where shear thinning effects are insignificant. There is already indirect evidence of this in Fig. 4, where data from BT (15) collapse onto a Newtonian master curve for  $\bar{\Omega}(\eta^{-1})$ . More directly, these previous studies used methyl celluloses with viscosity grade around 4,000 cP in the range of 0–0.3 wt.% (15) and at 0.18 wt.% (33). The shear thinning of such polymers has been measured (polymer AM4 in ref. 34) and fitted to a power law:  $\eta \sim \dot{\gamma}^{n-1}$ ; at  $c = 0.25$  wt.% and 0.5 wt.%,  $n = 1.00$  and 0.961,

respectively. Thus, at the concentrations used before (15, 33), shear thinning is very weak or absent, and the solutions behave as Newtonian.

## Summary and Conclusions

We measured the average swimming speed and cell body rotation rate in populations of *E. coli* bacteria swimming in different concentrations of solutions of the linear polymer PVP (nominal molecular weights of 10, 40, 160, and 360 kDa, these probably were number-averaged values) and the branched polymer Ficoll (70 and 400 kDa). We dialyzed each polymer to remove small-molecular impurities that can be metabolized by the cells to increase their swimming speed. The collapse of data for all polymers except PVP360k onto a single proportionality relationship between swimming speed and body rotation rate,  $\bar{\Omega}(\bar{v})$  (Fig. 3), demonstrates that these solutions behave as Newtonian fluids as far as *E. coli* propulsion is concerned.

Significant nonlinearities in  $\bar{\Omega}(\bar{v})$  were found for *E. coli* swimming in PVP360k solutions. Further analysis showed that the motion of the cell body remained Newtonian: the measured  $\bar{\Omega}(\eta^{-1})$  can be fitted to results derived from Newtonian hydrodynamics (Eqs. 10a and 10b; Fig. 5). Thus, there must be non-Newtonian effects at the flagellum. The observed deviations from Newtonian behavior can be quantitatively accounted for by a simple model in which the flagellum sees the viscosity of pure buffer. This result is consistent with significant shear thinning observed at the micrometer level in PVP360k solutions using microrheology, although we suggest that molecular effects must be taken into account because the polymer and flagellum filament have similar, nanometric dimensions. The effects we are considering, which arise from high shear rates, are absent from experiments using macroscopic helices as models for viscoelastic flagella propulsion (13).

Shear thinning is not the only possible effect in the vicinity of a flagellum creating local deformation rates of  $\sim 10^4 \text{ s}^{-1}$ . Higher-molecular-weight polymers that are more viscoelastic than PVP 360 kDa will show significant elastic effects. Interestingly, it is known that double-stranded DNA could be cut at a significant rate at  $\dot{\gamma} \sim 10^4 \text{ s}^{-1}$  (35). An *E. coli* swimming through a high-molecular-weight DNA solution should therefore leave behind a trail of smaller DNA and therefore of lower-viscosity solution, making it easier for another bacterium to swim in the wake. The latter may have important biomedical implications: the mucosal lining of normal mammalian gastrointestinal tracks and of diseased lungs can contain significant amounts of extracellular DNA. Exploration of these issues will be the next step in seeking a complete understanding of flagellated bacterial motility in polymeric solution.

## Materials and Methods

**Cells.** We cultured K12-derived WT *E. coli* strain AB1157 as previously detailed (21, 22). Briefly, overnight cultures were grown in Luria-Bertani (LB) broth using a shaking incubator at 30 °C and shaking speed of 200 rpm. A fresh culture was inoculated as 1:100 dilution of overnight grown cells in 35 mL tryptone broth (TB) and grown for 4 h (to late exponential phase). Cells were washed three times with motility buffer (MB, pH = 7.0, 6.2 mM  $\text{K}_2\text{HPO}_4$ , 3.8 mM  $\text{KH}_2\text{PO}_4$ , 67 mM NaCl, and 0.1 mM EDTA) by careful filtration (0.45- $\mu\text{m}$  HATF filter; Millipore) to minimize flagellar damage and were resuspended in MB to variable cell concentrations.

### Polymers.

**Native.** PVP and Ficoll from Sigma-Aldrich were used at four (10, 40, 160, and 360 kDa) and two (70 and 400 kDa) nominal molecular weights, respectively. Polymer stock solutions were prepared and diluted with MB.

**Dialysis.** The polymer stock solutions were dialyzed in tubes with 14-mm-diameter and 12-kDa cutoff (Medicell International) against double-distilled water. The dialysis was performed over 10 d with daily exchange of the water. The final polymer concentration was determined by measuring the weight loss of a sample during drying in an oven at 55 °C and subsequent vacuum

treatment for 6 h. Polymer solutions at several concentration were prepared by dilution using MB.

**Motility Measurement.** Bacterial suspensions were gently mixed with the polymer solutions to a final cell density of  $\approx 5 \times 10^8$  cells/mL. An  $\approx 400$ - $\mu\text{m}$ -deep flat glass sample cell was filled with  $\approx 150$   $\mu\text{L}$  of suspension and sealed with petroleum jelly to prevent drift. Immediately after, two movies, one in phase-contrast illumination ( $\sim 40$  s long, Nikon Plan Fluor 10 $\times$ Ph1 objective, NA = 0.3, Ph1 phase-contrast illumination plate at 100 frames/s and 500<sup>2</sup> pixels) and one in dark-field illumination ( $\sim 10$  s long, Nikon Plan Fluor 10 $\times$ Ph1 objective, NA = 0.3, Ph3 phase-contrast illumination plate, either 500 or 1,000 frames/s, 500<sup>2</sup> pixels) were consecutively recorded on an inverted microscope (Nikon TE300 Eclipse) with a Mikrotron high-speed camera (MC 1362) and frame grabber (Inspecta 5, 1-Gb memory) at room temperature ( $22 \pm 1$  °C). We image at 100  $\mu\text{m}$  away from the bottom of the capillary to avoid any interaction with the glass wall.

We measured the swimming speed from the phase contrast movies using the method of DDM as detailed previously (21, 22). The dark field movies were analyzed to measure the body rotation speed using the method of DFM, in which we Fourier transform the power spectrum of the flickering image of individual cells, and identify the lowest frequency peak in the average power spectrum (Fig. S9) as the body rotation frequency as in

previous work (24, 36); the difference here is that DFM is a high-throughput method (SI Text).

**Rheology.** We measured the low-shear viscosity  $\eta$  of polymer solutions using a TA Instruments AR2000 rheometer in cone-plate geometry (60 cm, 0.5°). Passive microrheology was performed using diffusing wave spectroscopy in transmission geometry with 5-mm-thick glass cuvettes. The setup (LS Instruments) uses an analysis of the measured mean square displacement (MSD) of tracer particles as detailed previously (37). Tracer particles (980-nm-diameter polystyrene) were added to the samples at 1 wt% concentration. The transport mean free paths  $l^*$  of the samples were determined by comparing the static transmission to a reference sample (polystyrene with 980 nm diameter at 1 wt% in water). The shear rate-dependent viscosity  $\eta$  was obtained from the frequency dependent storage and loss moduli using the Cox–Merz rule (27).

**ACKNOWLEDGMENTS.** This work was funded by the UK Engineering and Physical Sciences Research Council (EP/D071070/1, EP/I004262/1, and EP/J007404/1), EU 7th Framework Programme (PIIF-GA-2010-276190), European Soft Matter Infrastructure (262348), European Research Council (AdG 340877 PHYSAPS), Swiss National Science Foundation (PBRFP2-127867), and the Rowland Institute at Harvard.

1. Voynow JA, Rubin BK (2009) Mucins, mucus, and sputum. *Chest* 135(2):505–512.
2. McGuckin MA, Lindén SK, Sutton P, Florin TH (2011) Mucin dynamics and enteric pathogens. *Nat Rev Microbiol* 9(4):265–278.
3. Druart X (2012) Sperm interaction with the female reproductive tract. *Reprod Domest Anim* 47(Suppl 4):348–352.
4. Schreiber S, et al. (2004) The spatial orientation of *Helicobacter pylori* in the gastric mucus. *Proc Natl Acad Sci USA* 101(14):5024–5029.
5. Sanchez S, Hofacre CL, Lee MD, Maurer JJ, Doyle MP (2002) Animal sources of salmonellosis in humans. *J Am Vet Med Assoc* 221(4):492–497.
6. Houry A, et al. (2012) Bacterial swimmers that infiltrate and take over the biofilm matrix. *Proc Natl Acad Sci USA* 109(32):13088–13093.
7. Ndesendo VMK, et al. (2008) A review of current intravaginal drug delivery approaches employed for the prophylaxis of HIV/AIDS and prevention of sexually transmitted infections. *AAPS PharmSciTech* 9(2):505–520.
8. Lauga E, Powers TR (2009) The hydrodynamics of swimming microorganisms. *Rep Prog Phys* 72(9):096601.
9. Lauga E (2007) Propulsion in a viscoelastic fluid. *Phys Fluids* 19(8):083104.
10. Teran J, Fauci L, Shelley M (2010) Viscoelastic fluid response can increase the speed and efficiency of a free swimmer. *Phys Rev Lett* 104(3):038101.
11. Fu HC, Powers TR, Wolgemuth CW (2007) Theory of swimming filaments in viscoelastic media. *Phys Rev Lett* 99(25):258101.
12. Leshansky AM (2009) Enhanced low-Reynolds-number propulsion in heterogeneous viscous environments. *Phys Rev E Stat Nonlin Soft Matter Phys* 80(5 Pt 1):051911.
13. Liu B, Powers TR, Breuer KS (2011) Force-free swimming of a model helical flagellum in viscoelastic fluids. *Proc Natl Acad Sci USA* 108(49):19516–19520.
14. Schneider WR, Doetsch RN (1974) Effect of viscosity on bacterial motility. *J Bacteriol* 117(2):696–701.
15. Berg HC, Turner L (1979) Movement of microorganisms in viscous environments. *Nature* 278(5702):349–351.
16. Magariyama Y, Kudo S (2002) A mathematical explanation of an increase in bacterial swimming speed with viscosity in linear-polymer solutions. *Biophys J* 83(2):733–739.
17. Rubinstein M, Colby RH (2003) *Polymer Physics* (Oxford Univ Press, Oxford, UK).
18. Purcell EM (1997) The efficiency of propulsion by a rotating flagellum. *Proc Natl Acad Sci USA* 94(21):11307–11311.
19. Sowa Y, Berry RM (2008) Bacterial flagellar motor. *Q Rev Biophys* 41(2):103–132.
20. Bühler V (1998) *Kollidon: Polyvinylpyrrolidone for the Pharmaceutical Industry* (BASF Ludwigshafen, Germany), 4th Ed.
21. Wilson LG, et al. (2011) Differential dynamic microscopy of bacterial motility. *Phys Rev Lett* 106(1):018101.
22. Martinez VA, et al. (2012) Differential dynamic microscopy: A high-throughput method for characterizing the motility of microorganisms. *Biophys J* 103(8):1637–1647.
23. Schwarz-Linek J, et al. (2012) Phase separation and rotor self-assembly in active particle suspensions. *Proc Natl Acad Sci USA* 109(11):4052–4057.
24. Chattopadhyay S, Moldovan R, Yeung C, Wu XL (2006) Swimming efficiency of bacterium *Escherichia coli*. *Proc Natl Acad Sci USA* 103(37):13712–13717.
25. Larson RG (2005) The rheology of dilute solutions of flexible polymers: Progress and problems. *J Rheol (NY)* 49(1):1–70.
26. Huang C-C, Winkler RG, Sutmoller G, Gompper G (2010) Semidilute polymer solutions at equilibrium and under shear flow. *Macromol* 43(23):10107–10116.
27. Cox WP, Merz EH (1958) Correlation of dynamic and steady-flow viscosities. *J Polym Sci Polym Phys Ed* 28(118):619–622.
28. Montenegro-Johnson TD, Smith DJ, Loghin D (2013) Physics of rheologically enhanced propulsion: Different strokes in generalized Stokes. *Phys Fluids* 25(8):081903.
29. Velez-Cordero JR, Lauga E (2013) Waving transport and propulsion in a generalized Newtonian fluid. *J Non-Newton Fluid Mech* 199(09):37–50.
30. Cribb JA, et al. (2013) Nonlinear signatures of entangled polymer solutions in active microbead rheology. *J Rheol (NYYNY)* 57:1247.
31. Squires TM, Brady JF (2005) A simple paradigm for active and nonlinear microrheology. *Phys Fluids* 17(7):073101.
32. Caruso MM, et al. (2009) Mechanically-induced chemical changes in polymeric materials. *Chem Rev* 109(11):5755–5798.
33. Darnton NC, Turner L, Rojevsky S, Berg HC (2007) On torque and tumbling in swimming *Escherichia coli*. *J Bacteriol* 189(5):1756–1764.
34. Edelby Y, Balaghi S, Senge B (2014) Flow and Sol-Gel behavior of two types of methylcellulose at various concentrations. *AIP Conference Proceedings* 1593(1):750–754.
35. Adam RE, Zimm BH (1977) Shear degradation of DNA. *Nucleic Acids Res* 4(5):1513–1537.
36. Lowe G, Meister M, Berg HC (1987) Rapid rotation of flagellar bundles in swimming bacteria. *Nature* 325(2):637–640.
37. Mason TG (2000) Estimating the viscoelastic moduli of complex fluids using the generalized Stokes-Einstein equation. *Rheol Acta* 29(4):371–378.

# Supporting Information

Martinez et al. 10.1073/pnas.1415460111

## SI Text

**Predictions from Magariyama and Kudo.** We calculated the predicted dependence of swimming velocity on polymer concentration using the theory of Magariyama and Kudo (1) (Fig. S1) and show that, as they claimed, there is a peak. However, we also show a calculation that they did not report, namely, the predicted dependence of body rotation frequency as a function of polymer concentration. The latter is a rapidly increasing function, which is clearly unphysical and contradicts the observation by BT (2), as well as data shown here (Fig. 4).

## Characterizing the PVP.

**Intrinsic viscosity and overlap concentration.** The viscosity of a polymer solution at low concentrations can be written as a virial expansion of  $\eta$  in  $c$

$$\eta = \eta_s \left( 1 + [\eta]c + k_H[\eta]^2 c^2 + \dots \right), \quad [\text{S1}]$$

where  $[\eta]$  and  $k_H$  are the intrinsic viscosity and the Huggins coefficient, respectively, and  $\eta_s$  is the viscosity of the solvent, which here is motility buffer. The linearity at low  $c$  can be expressed in two different ways

$$\frac{\eta - \eta_s}{\eta_s c} = [\eta] + k_H[\eta]^2 c \quad (\text{Huggins}), \quad [\text{S2}]$$

$$\frac{\ln(\eta/\eta_s)}{c} = [\eta] + \left( k_H - \frac{1}{2} \right) [\eta]^2 c \quad (\text{Kraemer}). \quad [\text{S3}]$$

These two linear plots should extrapolate to  $[\eta]$  at  $c=0$ . The intrinsic viscosity measures the volume of a polymer coil normalized by its molecular weight, so that  $c^* \approx [\eta]^{-1}$ . A modern text names this as the best experimental method for estimating the overlap concentration (3).

We first regraph the  $\eta(c)$  data given by SD (4) as HK plots (Fig. S2A). For here and below, concentrations in wt% and grams per deciliter are interchangeable at the sort of concentrations we are considering. It is clear that their lowest  $c$  data point must be inaccurate. Discarding this point gives the expected linear dependence in both plots and a uniquely extrapolated value of  $[\eta] = 1.055$  at  $c=0$ , giving  $c^* = 0.95$  g/dL. Reference to our  $c^*$  values below suggests that SD's PVP360k has somewhat lower molecular weight than our material with the same label.

According to current industry standards (5), PVP360k should have viscosities of  $\approx 3$ – $5$  and  $\approx 300$ – $700$  mPa·s at 1 and 10 wt.% in water, respectively. SD's reported viscosities at 1 and 10 wt.% at 2.5 and 249 Pa·s, respectively, are lower than these values, again consistent with their material having lower molecular weight than our PVP360k.

We characterized all four PVPs used in this work by measuring their low-shear viscosity in motility buffer as a function of concentration. For PVP360k (K-90) at 1 and 10 wt.%, we found  $\eta \approx 4$  and 370 mPa·s, agreeing well with the published standards (5). We now graph the measured viscosities of our four PVPs at low concentrations as HK plots (Fig. S2 B–E). In each case, the expected behavior is found; the extrapolated values of  $[\eta]$  and the overlap concentrations calculated from these are given in Table S1. The scaling of  $[\eta]$  vs.  $M$  is consistent with a power law (Fig. S2F)  $[\eta] \sim M^a$ , with  $a = 0.781$ . Because  $[\eta] \approx r^3/M$ ,  $r \sim M^\nu$  with  $\nu = (1+a)/3$ . We find  $\nu = 0.593$ , which is consistent with the

renormalization group value of  $\nu = 0.588$  for a linear polymer in a good solvent.

**Coil radii, second virial coefficient, and molecular weight.** We performed static and dynamic light scattering (SLS and DLS, respectively) experiments to measure the radius of gyration,  $R_g$ , the molecular weight,  $M_w$ , the second virial coefficient,  $A_2$ , and the hydrodynamic radius,  $R_h$ , of PVP360k in water and motility buffer (6).  $R_h$  was measured by DLS, and  $R_g$ ,  $M_w$ , and  $A_2$  were measured using the Zimm plot of SLS data. Results are summarized in Table S2. The positive  $A_2$  is consistent with our conclusion above that water is a good solvent for PVP. There may be a mild degree of aggregation in motility buffer (larger radii and slightly smaller  $A_2$ ).

**Native Polymer Results.** Fig. S3A shows  $\bar{v}$  and  $\bar{\Omega}$  vs. polymer concentration,  $c$ , for as-bought, or native, PVP360k. Although  $\bar{\Omega}(c)$  decays monotonically, a peak is observed in  $\bar{v}$  at  $c \approx 0.5$ wt%, or roughly  $c^*$  for this molecular weight. The latter ostensibly reproduces SD's observations (4): their data are also plotted in Fig. S3A. In native PVP160k (Fig. S3B), the peak in  $\bar{v}(c)$  broadens, and now there is a corresponding broad peak in  $\bar{\Omega}(c)$  as well. These peaks broaden out into plateaus for native PVP40k and PVP10k (Fig. S3 C and D). We also performed experiments with native Ficoll with the manufacturer-quoted molecular weights of 70k and 400k and observed similar nonmonotonic, broadly peaked responses in both  $\bar{v}(c)$  and  $\bar{\Omega}(c)$  (Fig. S4).

**The Effect of Small-Molecule Energy Sources.** Here we show  $\bar{v}(c)$  for *E. coli* swimming in glycerol solutions of a range of concentrations (Fig. S5). The plot is indeed reminiscent of what is seen for native PVP10k and PVP40k. Indeed, we suggest that the increases at low concentrations in all four polymers have the same origin as the increase observed at low glycerol concentration: the availability of a small-molecule energy source. The decrease at high glycerol is an osmotic effect (as observed for other small molecules, e.g., sucrose) (7), whereas that seen in the 10k, 40k, and 160k polymers can be entirely accounted for by low-Re Newtonian hydrodynamics (polymeric osmotic effects at our concentrations are negligible).

**Dialyzed Ficoll Results.** Swimming speed and body rotation frequency as a function of concentration are shown for two purified Ficolls in Fig. S6.

## Shear-Thinning Calculations.

**Predicting  $\Omega(v)$  for flagellum experiencing buffer viscosity.** Here we outline the procedure used to calculate the rotation rate of the cell body for a bacterium swimming in shear-thinning PVP360k solution as a function of the swimming speed. We assume that the flagellum sees a viscosity  $\eta'$  that is different from the low-shear-rate viscosity  $\eta$  experienced by the bacterial body. This assumption is partly motivated by bulk and microrheological measurements (Fig. 6), showing that at the shear rates generated by the flagellum, shear thinning can be expected at least down to the micrometer scale. Empirically, the low- and high-shear viscosities plotted in Fig. 6 can be fitted by

$$\begin{cases} \eta_{\text{low-shear}} = -5.32 + 6.33 \exp(0.39c) & \dot{\gamma} \rightarrow 0 \text{ s}^{-1}, \\ \eta_{\text{high-shear}} = 0.96 + 0.69c + 0.44c^2 & \dot{\gamma} = 10^4 \text{ s}^{-1}, \end{cases} \quad [\text{S4}]$$

where  $c$  is in wt% and  $\eta$  in centipoise (cP).

In this two-viscosity model, the force and torque balance equations solve to Eq. S13

$$\frac{\Omega}{v} = \frac{\hat{d} \left[ \left( \frac{\eta}{\eta'} \right) \hat{a}_0 + \hat{a} \right] - \hat{b}^2}{\left( \frac{\eta}{\eta'} \right) \hat{d}_0 \hat{b}}. \quad \text{[S5]}$$

The friction coefficients in Eq. S5 are given by (8)

$$\hat{a} = k_n L \sin \psi \tan \psi (1 + \gamma \cot^2 \psi), \quad \text{[S6]}$$

$$\hat{b} = k_n L \frac{\lambda}{2\pi} \sin \psi \tan \psi (1 - \gamma), \quad \text{[S7]}$$

$$\hat{d} = k_n L \left( \frac{\lambda}{2\pi} \right)^2 \sin \psi \tan \psi (1 + \gamma \cot^2 \psi), \quad \text{[S8]}$$

$$\hat{a}_0 = \frac{4\pi b}{\ln \frac{2b}{a} - \frac{1}{2}}, \quad \text{[S9]}$$

$$\hat{d}_0 = \frac{16\pi}{3} a^2 b, \quad \text{[S10]}$$

where

$$k_n = \frac{8\pi}{2 \ln \frac{c\lambda}{r} + 1}, \quad \text{[S11]}$$

$$k_t = \frac{4\pi}{2 \ln \frac{c\lambda}{r} - 1}, \quad \text{[S12]}$$

and  $\gamma = k_t/k_n$ . Here,  $L = 7 \mu\text{m}$  and  $\lambda = 2 \mu\text{m}$  are the total length and pitch of the flagellum, respectively,  $\psi = 41^\circ$  is the angle made by the flagellar filament with the flagellar axis,  $r = 20 \text{ nm}$  is the estimated radius of the composite filament in a flagella bundle, and  $c = 2.4$  is the Lighthill constant. All parameters are taken from a previous experimental paper (8), where this set of parameters were shown to be consistent with the Purcell model.

Using the measured values of  $\bar{\Omega}(c)$  for PVP360k,  $\eta' = \eta_s$ ,  $\eta = \eta_{\text{low-shear}}$ , and Eq. S5 is sufficient to calculate the corresponding  $\bar{v}(\bar{\Omega})$ . Results show good agreement with the measured values (Fig. 3), thus predicting a peak in the swimming velocity on an increase in the viscosity of the polymer solution. For a better

illustration, we compare the predicted and measured values of  $\bar{v}$  as a function of the viscosity experienced by the body ( $\eta_{\text{low-shear}}$ ) in Fig. S7. Our theory is successful in predicting a peak in the swimming velocity in the right position and of the right shape.

**Deducing the viscosity the flagellum sees from measurements.** Now we relax our previous assumption that  $\eta'$  is equal to the viscosity of the solvent, and use Eq. S5 to extract the viscosity of the fluid surrounding the flagellar filament. Using the measured values of  $\bar{\Omega}(c)$  and  $\bar{v}(c)$ , Eq. S5 can be solved for  $\eta'$ . The results are shown in Fig. 6. Indeed, for most of the concentration range studied,  $\eta' \approx \eta_s$ .

**Dark-Field Flicker Microscopy.** Under dark-field illumination, the image of a swimming bacterium appears to flicker. By calculating the power spectrum of the spatially localized time-dependent intensity fluctuations of low-magnification images of a quantized pixel box (containing approximately one cell) and then averaging over all cells in the images, we are able to measure the body rotational frequency  $\Omega/2\pi$  averaged over  $\sim 10^4$  cells based on a  $\lesssim 10$ -s movie. This method is similar to what was done by Lowe et al. (9), who measured the power spectrum of single swimming cells. However, here we use low-magnification dark-field imaging, which allows high-throughput measurement of  $\Omega/2\pi$ .

Dark-field movies were recorded (Nikon Plan Fluor 10 $\times$ Ph1 objective, NA = 0.3, Ph3 phase-contrast illumination plate) at either 500 or 1,000 Hz on an inverted microscope (Nikon TE300 Eclipse) with a Mikrottron high-speed camera (MC 1362) and frame grabber (Inspecta 5, 1-Gb memory) at room temperature ( $22 \pm 1^\circ\text{C}$ ). The images correspond to an area of  $\approx 720 \times 720 \mu\text{m}$ , containing around  $10^4$  bacteria. Approximately 4,000 frames were captured, at a resolution of  $512 \times 512$  pixels.

To process a video sequence, each frame was divided into square tiles of side length  $l$  (typically five pixels), and the pixel values in each tile were summed to give a single number. This process was repeated for every frame in the video sequence, yielding intensity as a function of time for each tile. The power spectrum of these data was calculated for each tile separately, before averaging over all tiles to give smoothed data for the whole video sequence. The power spectrum is then normalized by the frequency squared to remove any contribution from Brownian motion due to the nonmotile cells, inherently present in the bacterial suspensions. An example is shown in Fig. S9. We identify the first peak as the body rotational frequency  $\Omega/2\pi$  in line with previous studies (9).

**Viscosity Measurements.** The viscosity of PVP360k measured using conventional rheometry and DWS microrheology (*Materials and Methods*) at different concentrations is shown in Fig. S8. There is reasonable overlap between the two methodologies at intermediate shear rates.

- Magariyama Y, Kudo S (2002) A mathematical explanation of an increase in bacterial swimming speed with viscosity in linear-polymer solutions. *Biophys J* 83(2):733–739.
- Berg HC, Turner L (1979) Movement of microorganisms in viscous environments. *Nature* 278(5702):349–351.
- Rubinstein M, Colby RH (2003) *Polymer Physics* (Oxford Univ Press, Oxford, UK).
- Schneider WR, Doetsch RN (1974) Effect of viscosity on bacterial motility. *J Bacteriol* 117(2):696–701.
- Bühler V (1998) *Kollidon: Polyvinylpyrrolidone for the Pharmaceutical Industry* (BASF, Ludwigshafen, Germany), 4th Ed.

- Berne BJ, Pecora R (2000) *Dynamic Light Scattering* (Dover Publications, New York).
- Pilizota T, Shaevitz JW (2013) Plasmolysis and cell shape depend on solute outer-membrane permeability during hyperosmotic shock in *E. coli*. *Biophys J* 104(12):2733–2742.
- Chattopadhyay S, Moldovan R, Yeung C, Wu XL (2006) Swimming efficiency of bacterium *Escherichia coli*. *Proc Natl Acad Sci USA* 103(37):13712–13717.
- Lowe G, Meister M, Berg HC (1987) Rapid rotation of flagellar bundles in swimming bacteria. *Nature* 325(2):637–640.







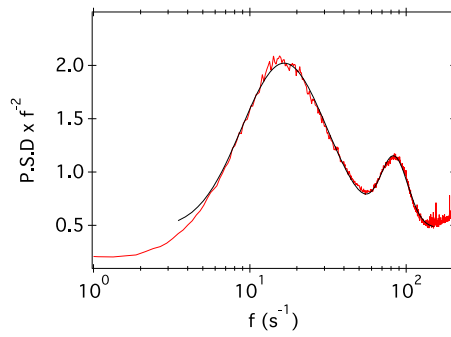


**Fig. S9.** Typical example of the power spectrum of the flickering dark-field image of individual cells averaged over  $\approx 10^4$  cells based on an  $\approx 10$ -s dark-field movie (*Materials and Methods*). The power spectrum is normalized by the frequency square to remove contribution from Brownian motion due to the inherent presence of nonmotile cells in the suspension. The black line corresponds to a two-peak fit using Lognormal distribution.

**Table S1. Intrinsic viscosity,  $[\eta]$ , and Huggins coefficient,  $k_H$ , obtained by fitting simultaneously (global fitting) the viscosity data using both Huggins and Kraemer equations**

Solutions	$[\eta]$ (dL/g)	$k_H$	$c^*$ (g/dL or wt%)
PVP360k	$1.84 \pm 0.04$	$0.38 \pm 0.02$	$0.55 \pm 0.01$
PVP160k	$0.72 \pm 0.01$	$0.38 \pm 0.01$	$1.40 \pm 0.02$
PVP40k	$0.263 \pm 0.003$	$0.38 \pm 0.02$	$3.8 \pm 0.1$
PVP10k	$0.105 \pm 0.006$	$0.42 \pm 0.08$	$9.5 \pm 0.5$
SD (4)	$1.05 \pm 0.02$	$0.38 \pm 0.02$	$0.95 \pm 0.02$

**Table S2. Parameters obtained from SLS and DLS for PVP360k in water or in motility buffer (MB)**

Solutions	$M_w$ (g/mol)	$A_2$ (mol L/g <sup>2</sup> )	$R_g$ (nm)	$R_h$ (nm)
PVP360k in water	$840 \times 10^3$	$3.0 \times 10^{-7}$	56	30
PVP360k in MB	$1,500 \times 10^3$	$2.6 \times 10^{-7}$	79	37